RSC Advances

ROYAL SOCIETY OF CHEMISTRY

www.rsc.org/advances

Enhanced photocatalytic degradation of methylene blue and adsorption of arsenic (III) by reduced graphene oxide (rGO)-metal oxide (TiO_2/Fe_3O_4) based nanocomposites

Poonam Benjwal[a], Manish Kumar[b], Pankaj Chamoli[a] and Kamal K. Kar[a,b*]

[a]Advanced Nanoengineering Materials laboratory, Materials Science Programme, Indian Institute of Technology Kanpur, Kanpur-208016, India

[b]Advanced Nanoengineering Materials laboratory, Department of Mechanical Engineering, Indian Institute of Technology Kanpur, Kanpur-208016, India

*Corresponding author. Fax: +91-512-2597408; E-mail address: kamalkk@iitk.ac.in (Kamal.K.Kar)

Abstract

The reduced graphene oxide (rGO) and metal oxide based binary (rGO-TiO_2/rGO-Fe_3O_4) and ternary (rGO-Fe_3O_4-TiO_2) nanocomposites with enhanced photocatalytic and adsorption properties are successfully synthesized by simple one-step solvothermal process. The microscopy images of nanocomposites show that the ferric oxide (Fe_3O_4) and titania (TiO_2) nanoparticles are firmly anchored over rGO, which enhances the surface area of resultant nanocomposites. The as-synthesized nanocomposites are evaluated for the removal of methylene blue dye under UV and visible light irradiation as well as for the adsorption of As(III) from the aqueous solution. Compared to binary, the ternary (rGO-Fe_3O_4-TiO_2) nanocomposite exhibits highest dye degradation efficiency (~100% within 5 minutes). This enhancement is attributed to the synergetic interaction and increase in surface area of rGO-Fe_3O_4-TiO_2. For As(III) adsorption, the adsorption data are obtained by Langmuir and Freundlich adsorption isotherms. Compared to binary nanocomposites, the maximum monolayer adsorption capacity (147.05 mg/g) is observed for rGO-Fe_3O_4-TiO_2. These results reveal that the rGO-Fe_3O_4-TiO_2 nanocomposite has potential application in water/wastewater treatment.

Keywords: Water pollution, Graphene oxide, Nanocomposite, Photocatalysis, Adsorption

1. Introduction

The rapid development of industries has introduced many serious problems to ecosystem and aquatic atmosphere, leading to the deterioration of environment and health of human beings. The industrial discharged water contains many harmful contaminations such as heavy metals and dyes, which are considered very carcinogenic to human health. Thus, several methods like chemical precipitation, coagulation, membrane filtration, ion exchange, adsorption, photocatalysis, etc. have been developed for the removal of contaminations from industrial wastewater [1-4]. Among them, adsorption and photocatalysis based remediation process are widely accepted due to their low cost and ease of processing. Recently, graphene, a 2-D honeycomb structure of single layer sp^2-bonded carbon atoms, has been extensively investigated for wastewater purification treatment mainly due to its large surface area, high charge carrier mobility, high adsorption capacity and excellent electron transfer rate, which makes it preferable for supporting metal oxides towards the several environmental remediation [5-8]. However, the water insoluble properties of graphene limit its wide use in water purification [9]. In addition, the π- π interaction between the adjacent sheets of graphene leads to the loss of effective surface area and adsorption capabilities. Graphene oxide (GO), the oxidized derivative of graphene, comprise of various functional groups such as carboxyl, hydroxyl and epoxide on its surface, which makes it highly hydrophilic and water soluble and thus making it applicable for supporting metal/metal oxides particles [10]. Thus, the incorporation of metal oxides on GO has become a proficient way to prepare the environment friendly composite, where the metal oxide improves its properties by utilizing the advantage of graphene [7, 11, 12]. However, the direct separation of GO from a well dispersed solution through centrifugation or filtration is a tedious process as GO gets easily aggregate, which can reduce the adsorption efficiency [13]. Thus to improve the adsorption efficiency of GO the incorporation of the magnetic adsorbents on graphene-based materials has received much attention as after purification process, magnetic adsorbents

incorporated graphene/GO materials can be easily separated from the suspension using magnetic field [14]. Compared to other magnetic adsorbents, Fe_3O_4 is the most noticeable metal oxide due to its highly reactive surface and large surface area, cost efficiency, and less-toxicity [15]. The incorporation of Fe_3O_4 nanoparticles on GO prevents the aggregation and reassembling of graphene sheets, which results larger surface area of hybrid nanostructure [16]. Moreover, Fe_3O_4 nanoparticles particularly possess high adsorption affinity towards hazardous water pollutants and also facilitate a convenient magnetic separation for recycle/removal of nanocomposite with the application of external magnet by owing inherently super magnetic property [17]. Furthermore, for the removal of toxic organic impurities from water TiO_2, a wide band gap semiconductor, is widely used due to its high photo catalytic and antibacterial activity, low-cost, chemical stability, and non-toxicity [18]. However, the high recombination rate of electron-hole pairs limits TiO_2 efficiency as an efficient photocatalyzer. It has been observed that TiO_2 nanocrystalline growth on graphene sheet promotes transfer of electrons from the conduction band of TiO_2 to graphene sheet via percolation mechanism [19]. In this case, electron transfer leads to the formation of heterojunction at the interface, which suppress the recombination of photo induced electron–hole pairs and thus enhances the photocatalytic performance of TiO_2-graphene composites. These TiO_2-graphene composites have been used in many applications such as photocatalysis, solar cells, and hydrogen evolution [20-22].

In the present study, we report a ternary nanocomposite, reduced graphene oxide-ferric oxide-titania (rGO-FeO_4-TiO_2), synthesized by simple wet assembling method for the removal of toxic methylene blue (MB) dye and As(III) from wastewater. During *in-situ* synthesis of GO/metal oxide nanocomposite, GO is reduced into the rGO. The rGO-FeO_4-TiO_2 nanocomposite consists the unique properties of each constituent such as, TiO_2 nanoparticles degrades the organic pollutant, rGO provides an effective pathway to increase the surface area as well as suppress the recombination of charge carriers in TiO_2, and Fe_3O_4, being a magnetic material, increases the

adsorption capabilities of rGO towards the heavy metal impurities and also helps in magnetic separation. To compare the properties of rGO-Fe_3O_4-TiO_2, the binary nanocomposites rGO-TiO_2 and rGO-Fe_3O_4 have been also prepared by solvothermal method. A systematic study has been done to investigate the photocatalytic activity under visible and UV light irradiation for MB dye and adsorption of As(III) metal ions by analyzing their adsorption isotherm and adsorption kinetics models, respectively.

2. Experimental

2.1 Materials and Methods

All the chemicals used in study were of analytical grade. Graphite powder and titanium tetraisobutoxide (TTIB; Ti $(OC_4H_9)_4$; were procured from Loba Chemie, India and Sigma-Aldrich respectively. Sulfuric acid (H_2SO_4, 98%), hydrogen peroxide (H_2O_2, 30%), potassium permanganate ($KMnO_4$), sodium nitrate ($NaNO_3$) and ethylene glycol ($C_2H_6O_2$) were purchased from Fisher Scientific, India, while ferric chloride hexahydrate ($FeCl_3.6H_2O$), acetic acid (Hac), sodium acetate (NaAc) and methylene blue dye were received from Loba Chemie India. Sodium arsenite ($NaAsO_2$), used as As(III) source, was obtained from SDFCL India. All chemicals were used without further purification.

GO was prepared by modified Hummer's method reported elsewhere [23]. The rGO-Fe_3O_4 nanocomposite was synthesized by solvothermal reaction reported elsewhere [24], while rGO-TiO_2 was also synthesized by simple solvothermal method [25]. The ternary composite rGO-Fe_3O_4-TiO_2 was synthesized by using wet chemical method. All the experimental procedures in detail are given in the supplementary information (S1).

2.2 Characterization

The crystalline phases of the graphite powder, GO, binary and ternary nanocomposites were analyzed through X-ray diffraction (XRD) using X'Pert Pro PANalytical, advanced X-Ray diffractometer with a Cu Kα adsorption spectrometer. Raman spectroscopy was recorded by

LabRam Micro-Raman spectrometer (Jobin-Yuon HR 800 UV) using a He-Ne (632.8 nm) laser excitation source. The morphology of GO and nanocomposites was examined by field emission scanning electron microscopy (FESEM; JEOL JSM-7100F). Fourier transform infrared spectroscopy (Bruker-FTIR) was conducted by using KBr pallet in the range of 4000-400 cm^{-1}. The absorbance properties of the nanocomposites were acquired by the UV–vis diffuse reflectance spectra (UV-vis DRS) with a UV–vis–NIR spectrophotometer (PerkinElmer Lambda 1050). The specific surface area and pore size distribution were calculated by the Brunauer-Emmett–Teller (BET) and Barrett-Joyner-Halenda (BJH), respectively with an automatic instrument Autosorb iQ (Quanta Chrome Instruments version 3.01). The chemical analysis of GO and nanocomposites were carried out by X-ray photoelectron spectroscopy (XPS) acquired with a PHI500 (Versa ProbeII, FEI Inc.) with Al Kα (1486.6eV) X-ray source. Batch adsorption analysis of As(III) metal ion was analyzed by atomic adsorption spectroscopy (Spectra A 220FS). The photocatalytic and adsorption experiments were carried out for MB and As(III), respectively. The detailed description of the photocatalytic setup and sample preparation for photocatalysis as well as for adsorption experiments are provided in the supplementary information (S1).

The photocatalytic degradation rate and removal efficiency of MB under visible and UV irradiation were calculated by measuring the absorbance of collected solutions by UV–vis spectrophotometer at λ_{max} ~664nm, which is usually determined by $\frac{C_0 - C_t}{C_0} \times 100\%$, where C_0 (initial) and C_t are the concentrations of MB at time (0) and (t), respectively. The uptake amount of As(III) by nanocomposites was calculated by $Q_e = \frac{V\,(q_0 - q_e)}{m}$, where q_0 and q_e are initial and equilibrium concentration of As(III) in mg L^{-1}, respectively, m is the weight of adsorbent in grams while V is the volume of solution in liter.

3. Results and discussion

The morphology and grain size of GO and binary/ternary nanocomposite were investigated by FESEM (Fig.1). The FESEM image of GO (Fig.1a) reveals a platelet-like porous three-dimensional interlinked structure, which forms due to the exfoliation and restacking process of GO, while the rGO-TiO_2 nanocomposite (Fig.1b) depicts a crinkled texture, where TiO_2 nanoparticles spread over the rGO sheet. The average grain size of the attached TiO_2 nanoparticles comes around 12 nm. These images also reveal the well dispersion and good anchoring of TiO_2 nanoparticles on rGO sheets, which ultimately increase the surface area of nanocomposites. Generally, due to the restacking the rGO sheets show a tendency to get aggregate back. But here, this aggregation is prevented due to the crystallization of TiO_2 on the surface of rGO [26]. In binary rGO-Fe_3O_4 nanocomposite (Fig.1c), the FESEM image shows that with few aggregations, the surface of rGO sheet is uniformly and densely anchored with Fe_3O_4 nanoparticle with a wide distribution of sizes ranging from 100 to 200 nm. Here, Fe_3O_4 nanoparticles of different sizes are dispersed on the both sides of the rGO, which can give a better magnetic response. Thus, the perfect anchoring and uniform dispersion of Fe_3O_4 nanoparticles on GO sheets prevent the agglomeration, which provide larger surface area and thus facilitate the electrons transfer process [27]. Moreover, no independent Fe_3O_4 nanoparticles outside the rGO sheets are observed, which implies that all the decorated nanoparticles are firmly attached to the surface. In case of rGO-Fe_3O_4-TiO_2 (Fig. 1d) the FESEM image reveals a crumpled and rippled type structure, which occurs due to the restacking of rGO sheets. Here, TiO_2 and Fe_3O_4 are uniformly attached to the surface of rGO. Additionally, the intimate connection between TiO_2-Fe_3O_4 and rGO facilitates the transfer of photo-induced electron during photoexcitation process, which enhances photo catalytic activity of nanocomposites [25]. The weight. % of the elements in nanocomposite has been evaluated by EDX (Fig.S1; Table S1), which firmly confirms the incorporation of Fe_3O_4 and TiO_2 in nanocomposites.

Fig 2 shows the XRD patterns of commercially obtained graphite powder, synthesized GO, binary and ternary nanocomposite. As revealed in Fig.2(a), graphite powder exhibits a sharp diffraction peak at 26.45°, corresponding to the interplanar spacing of 0.33 nm and a somewhat less intense peak at 54.52°. These peaks can be ascribed to the (002) and (004) hexagonal lattice planes of natural graphite, respectively. Fig.2(b) reveals the diffraction pattern of GO, which shows a little broad peak at 12.03°, corresponding to the interlayer spacing of ~0.73 nm, indicating the destruction of graphite structure due to the oxidation and thus confirms the conversion of graphite powder into GO [28]. The oxidation of graphite powder introduces numerous functional groups, which are bonded on the edges as well as both side of basal plane of the graphitic layer [29]. For solvothermal synthesized rGO-TiO_2 nanocomposite (Fig.2c), the XRD pattern displays sharp peaks at 25.3, 37.8, 48, 53.9 and 62.7 °, which are due to the (101), (004), (200), (105) and (204) tetragonal anatase phase of TiO_2, (*JCPDS* 21–1272), respectively. Here, rGO-TiO_2 nanocomposite does not show the characteristic peak of graphene at 26.4° (*d* ~0.34 nm), as it is masked by the strong peak of TiO_2 at 25.4° (101). This overlapping of graphene peak by TiO_2 confirms that the solvothermal process enhances the reduction of GO [30]. Subsequently, similarly synthesized rGO-Fe_3O_4 nanocomposite (Fig.2d) demonstrates the diffraction peaks at 30.6, 36.1, 43.7, 53.4, 57.6, and 63.1° of Fe_3O_4, which can be indexed to (220), (311), (400), (422), (511) and (440) planes (*JCPDS* 65-3107), respectively. Here, a less intense broad peak at 25.61° (d ~ 0.35 nm) is the characteristic peak of graphite, which confirms the reduction of GO after solvothermal process [31]. Further, rGO-Fe_3O_4–TiO_2 (Fig.2e) displays the characteristics peaks of antase phase of TiO_2 as well as of Fe_3O_4, which are anchored onto rGO sheet. This confirms the formation of ternary nanocomposite. Here, the broad weak peak of rGO at 25.25° (*d* ~0.35 nm) is superimposed by the strong peak of anatase TiO_2 at 25.4°. For all nanocomposites, the absence of GO peak implies the complete exfoliation and reduction of GO into rGO. Further, the broad diffraction peaks of binary and ternary nanocomposite imply the

small crystalline size of the Fe_3O_4/TiO_2 nanoparticles. Moreover, these results also suggest that during the synthesis of rGO-TiO_2 and rGO-Fe_3O_4-TiO_2 nanocomposite, TiO_2 precursor (TTIB) is converted into antase phase. To compare the XRD patterns of nanocomposites with TiO_2 and Fe_3O_4, the XRD patterns of them are attached in supporting information (Fig.S2), where the pristine TiO_2 shows pure anatase structure.

To further explore the chemical, structural and vibrational bands of nanocomposites, Raman study was carried out. Fig. 3 shows the Raman spectra of GO and binary/ternary nanocomposites, where GO (Fig.3a) shows two sharp peaks at 1341 and 1603 cm^{-1}, which can be attributed to the disorder carbon (D band) and graphitic carbon (G band), respectively [32]. A weak D band implies the low density of defects, whereas the crystal structure, disorder and defects can be analyzed with the change in relative intensity of D and G peaks [33]. Here, D and G band intensity ratio (I_D/I_G) is found ~1.13. The rGO-TiO_2 nanocomposite (Fig.3b) shows the specific vibration modes centered at 144 (E_g), 396 (B_{1g}), 512 (B_{1g} + A_{1g}) and 631 cm^{-1} (E_g), indicating the presence of the anatase phase of TiO_2 [18], which is consistent with the XRD results. Moreover, compared to GO, here I_D/I_G ratio increases to ~1.17, which indicates the removal of oxygen from GO. Further, rGO-Fe_3O_4 nanocomposite (Fig.3c), displays the characteristic peak of Fe_3O_4 at 223, 285, and 400 cm^{-1} [34] as well as the peaks of graphitic structure at D (1331 cm^{-1}) and G (1605 cm^{-1}), where the band intensity ratio (I_D/I_G) increases to ~1.21. This enhanced intensity ratio again confirms the removal of oxygen from GO. The Raman spectra of rGO-Fe_3O_4-TiO_2 (Fig.3d) shows the individual peaks of Fe_3O_4 (223, 285, 400 cm^{-1}), TiO_2 (144, 396, 512, 631 cm^{-1}) and rGO, having D and G band at 1329 and 1600 cm^{-1}, respectively. Here, the calculated I_D/I_G ratio comes around ~1.15, which is more than GO, which further affirms the removal of oxygen [35]. Further, the G band of rGO- Fe_3O_4-TiO_2 becomes weaker and broader, indicating the higher degree of defects in graphene due to the reduction of GO into rGO [36]. The increased ratio of I_D/I_G intensity in binary and ternary nanocomposites

also indicates the higher degree of defects, which generates due to incorporation of Fe_3O_4 and TiO_2 onto rGO sheets [37].

The strong acid interaction of graphite develops many oxygen-containing functional absorption groups. To evaluate the chemistry of these functional groups, FTIR of GO and as synthesized binary and ternary nanocomposite has been carried out in the range of 4000-400 cm^{-1} (Fig.4). The spectrum of GO (Fig.4a) shows the absorption stretching vibrations peaks, centered at 1060 and 1706 cm^{-1}, which can be ascribed to the stretching of C-O and C=O groups, while the vibration band at 1571-1210 cm^{-1} is due to the stretching of phenolic group C-OH and C=C group, respectively. Moreover, the broad peak at 3412 cm^{-1} arises due to the stretching vibrations of O-H stretching mode of intercalated water [38], whereas the small peaks at 2854 and 2921 cm^{-1} are attributed to the stretching vibration of the CH_2 bond [25]. In binary rGO-TiO_2 nanocomposite (Fig.4b), some of the functional groups such as OH, -COOH are removed due to the formation of Ti–O–C bond on the GO surface [39]. Here, the lowering of the absorption peak at 1705 cm^{-1} can be assigned to the C=O stretching. Moreover, the bands at 1400–1600 cm^{-1} can be accredited to the Ti-O-C vibration affirms the effective interaction between Ti and C, indicating the impregnation of TiO_2 on rGO while the absorption band at 670-450 cm^{-1} implies the presence of Ti-O-Ti bond on the surface of rGO-TiO_2 nanocomposite [40, 41]. In rGO-Fe_3O_4 nanocomposite (Fig.4c), most of the oxidized functional groups disappear, confirming the reduction of GO into rGO as the weakening of the absorption peaks at 1628 cm^{-1} and 1038 cm^{-1} indicates the reduction of GO, while the appearance of an additional band at 619-578cm^{-1} ensures the absorption of water due to Fe_3O_4 nanoparticles [36]. Further, the new characteristics peak, originates at 573 cm^{-1}, can be attributed to the stretching vibration of the Fe-O bond. Finally, the FTIR spectra of rGO-Fe_3O_4-TiO_2 (Fig.4d) clearly show the decrement of the absorption bands, with the characteristics peak of TiO_2 and Fe_3O_4 at 670 cm^{-1} and 578 cm^{-1},

respectively, which affirms that during solvothermal process TiO_2 and Fe_3O_4 nanoparticles have been covalently grafted over rGO sheets.

The specific surface area and pore size distribution of GO and nanocomposite were calculated by using BET and BJH, respectively. The N_2 adsorption/desorption isotherms were obtained at 77 K and prior to start the characterizations all the samples were degassed in N_2 for 8 h at 100^oC under vacuum. Multi-point BET surface area and BJH pore size distribution for each sample are shown in Table S2. It is evident from the Table S2 that compared to GO, the nanocomposites own a high surface area, where binary rGO-TiO_2 nanocomposite provides the highest specific surface area (246.27 m^2/g). The lowering of surface area in rGO-Fe_3O_4 may be attributed to the magnetic nature of Fe_3O_4 nanoparticles, due to which they can easily combine together [42]. The surface area of rGO-Fe_3O_4-TiO_2 comes around 173.10 m^2/g, which is more than that of rGO-Fe_3O_4 but less than that of rGO-TiO_2. Here, the reduction of surface area is due to the addition of Fe_3O_4. The BJH analysis confirms that the interlayered structure of nanocomposites forms an open porous structure, having a number of macro and meso pores. Here, the porous structure of nanocomposites can facilitate the diffusion of charge carriers, which is very essential for the photocatalytic degradation process.

The chemical states of GO and nanocomposites was evaluated by XPS. The peaks were analyzed by using XPSPEAK version 4.1 program, where Shirley background and Gaussian–Lorentzian distributions were employed to fit the baselines and XPS peaks, respectively. Fig.5a shows the survey spectra of GO, rGO-TiO_2, rGO-Fe_3O_4 and rGO-Fe_3O_4-TiO_2 nanocomposites, which confirm the presence of C1s, O1s, Fe2p and Ti2p in them. The XPS spectrum of C1s of GO (Fig.4b) consists the center peak at 284.5 eV, which originates from the graphitic sp^2 carbons, while the peaks at 286.6, 287.8 and 288.8 eV are due to the oxygenate group attached to the carbon atom, such as C-O, C=O and O-C=O groups, respectively [43]. However, in rGO-TiO_2, rGO-Fe_3O_4 and rGO-Fe_3O_4-TiO_2, most of the epoxide and hydroxide groups are removed from

C1s XPS spectrum (Fig 5c,e,g) and intensity of the peaks related to the oxygen functionalities becomes weaker than that of GO. The reduction of peak intensities affirms the presence of residual oxygenate group on rGO. It is observed that in nanocomposites the C/O ratio enhances, which indicates that the rGO sheets can serve as a conductive channel between the metal oxides nanoparticles and are favorable for photocatalytic process [36]. In rGO-TiO_2 (Fig.5c), the main broad peak at 284.3eV and other peaks at 285.6 and 287.9 eV are due to the residual oxygen containing groups. The presence of oxygenated weaker peak indicates the deoxygenation of GO and formation of rGO. The rGO-Fe_3O_4 provides the similar type of C1s spectra (Fig.5e), however compared to rGO-TiO_2, the intensity of peak centered at 284.3eV increases, which implies the enhancement of the remaining oxygenate groups. The presence of these bonds indicates the high degree of oxidation in GO, which occurs during the synthesis of GO by Hummers method. Again compared to GO, the respective peak intensities of C1s spectra of rGO-Fe_3O_4-TiO_2 nanocomposite (Fig. 5g) reduces, which implies that during solvothermal synthesis of ternary nanocomposite most of the hydroxyl and epoxide functional groups have been successfully removed. The removal of these groups indicates the good electronic conductivity among its constituents, which might induce the GO sheet to serves as a conductive channel between Fe_3O_4 and TiO_2 nanoparticles [36]. Fig 5(d) shows XPS spectra of Ti2p of the binary rGO-TiO_2, where the spin-orbit splitting of Ti2p peak leads the doublets Ti2p3/2 and Ti2p1/2, which are located at 457.3 and 463 eV, respectively. These peak positions also confirm that, here core level Ti^{4+} spectrum is of antase phase [18], which is the agreement with XRD and Raman analysis. However, in rGO-Fe_3O_4-TiO_2 (Fig.5h), the Ti2p3/2 (459 eV) and Ti2p1/2 (464.5 eV) peaks shift towards somewhat higher binding energy, which might be due to the formation Ti-O-Fe bonds on the surface of TiO_2. Moreover, the low binding energy difference between these doublets (5.5 eV) indicates the interaction between the lattice Ti and oxide functional groups of rGO [44]. Further, the high resolution XPS spectrum of Fe2p in rGO-Fe_3O_4 (Fig 5f) shows two

characteristics peaks of Fe2p3/2 (710.09 eV) and Fe2p1/2 (723.34 eV), which is accredited to the Fe(III). The Fe2p3/2 has associated satellite peak, which is situated around 8eV higher (717.53 eV) than the principal peak and does not overlap with Fe2p3/2 or Fe2p1/2 peak. This is in agreement with the reported XPS results [45]. This satellite peak is the characteristics of Fe^{3+} state of γ-Fe_2O_3 state. Moreover, the peak obtained at 709.09 confirms the oxidation of Fe^{2+} [46].

3.1 Photocatalytic activity of nanocomposites

The photo catalytic performance of rGO-TiO_2, rGO-Fe_3O_4 and rGO-Fe_3O_4-TiO_2 nanocomposites were evaluated by the degradation of MB in aqueous solution under UV and visible irradiation, both (Fig.6). For comparison, photocatalytic degradation was also carried out with bare TiO_2 and Fe_3O_4 nanoparticles. In visible light irradiation, it is observed that TiO_2 degrades 98% of MB dye within 100 min, while rGO-TiO_2 degrades almost all MB within 25 min (Fig.6a). Here, the low degradation efficiency of pure TiO_2 can be attributed to its high band gap as well as fast recombination rate of charge carriers. However, in rGO-TiO_2, the rGO sheets serve as the excellent electrons acceptor and thus help in the quick transfer of photo-induced electrons from the conduction band of TiO_2 to its surfaces [47]. This prevents the recombination of charge carriers and thus enhances the photocatalytic activity of rGO-TiO_2. Further, under UV light exposure, the degradation rate increases and rGO-TiO_2 completely removes the dye within 8 min, while pure TiO_2 takes 50 min for the same (Fig.6c). Here, the faster degradation of MB can be attributed to the increment of defect sites, leading to the better absorption of light. The whole photocatalytic mechanism of TiO_2 and binary rGO-TiO_2 nanocomposite for MB degradation is attached in the supporting information (S3). In addition, in presence of UV irradiation, H_2O_2 plays vital role in degradation of MB as it generates two hydroxyl radicals (HO•). The HO• are considered extremely strong oxidant for the degradation of organic pollutants [48]. Thus, the incorporation of H_2O_2 helps in MB degradation (S4).

The photocatalytic degradation characteristics of rGO-Fe_3O_4 and Fe_3O_4 for MB in presence of visible and UV light are displayed in Fig. 7. Generally, Fe_3O_4 exhibits the excellent adsorption capacity and its incorporation in rGO-Fe_3O_4 prevents the agglomeration and restacking of rGO, which eventually increases surface area and adsorption sites of nanocomposite [16]. In addition, the synergistic interaction between rGO and Fe_3O_4 makes the electron transfer easy, which can facilitate the reduction of Fe^{3+} to Fe^{2+}as well as generation of HO•. However, under visible light irradiation, a somewhat less degradation is observed (Fig.7a). The high catalytic activity of Fe_3O_4 and rGO-Fe_3O_4 under UV irradiation can be attributed to the enhanced photo-induced charge separation (Fig.7c) [49]. In addition, due to the suppression of charge recombination, rGO-Fe_3O_4 shows better photocatalytic activity than bare Fe_3O_4. The reaction mechanism of photocatalytic degradation of MB by Fe_3O_4 and rGO-Fe_3O_4 are described in the supporting information (S5). Moreover, in presence of H_2O_2, Fe_3O_4 nanoparticles initiate heterogeneous Fenton-like reaction, which further enhances adsorption rate due to the catalytic degradation of MB (S6).

The highest photocatalytic degradation efficiency for MB is observed for rGO-Fe_3O_4-TiO_2 nanocomposite (Fig.8), where it is found that in presence of UV irradiation, it degrades ~100% of MB under 5 min, while in visible light, 91% of MB eliminates (Fig.8a). Here, the enhancement in photocatalytic activity can be accredited to the synergic effect between catalytic activity and adsorption capability of nanostructured TiO_2 and Fe_3O_4 with rGO. Here, the degradation of MB can proceed by many ways such as direct attack of hydroxyl radical, direct reduction by photo-induced electron or direct oxidation in the presence of holes [50]. As, it is discussed earlier that rGO sheets show a tendency to get agglomerated back in graphitic structure due to strong van der Waal interaction [26]. Here, the incorporation of TiO_2 on the rGO surface helps to reduce the agglomeration of the graphene sheets. Moreover, during the photocatalysis process the interlink connection between TiO_2 and rGO permits the easy electrons transfer,

which can significantly enhances the charge carrier separation and hence improves the photocatalytic activity. Furthermore, in presence of H_2O_2 the incorporated Fe_3O_4 produces the excess HO• from Fenton/photo-Fenton processes, which can further degrades the adsorbed dye from the surface of the nanocomposite. Fe_3O_4 helps the pollutants to get adsorbed on the surface of nanocomposite, which eventually enhances the degradation rate. In addition, being a magnetic adsorbent, Fe_3O_4 favors in the magnetic separation of the nanocomposite photocatalyst from the dispersion. Thus, the incorporation of TiO_2 and Fe_3O_4 in rGO improves the photocatalytic activity of rGO-Fe_3O_4-TiO_2. The photocatalytic degradation of MB by all nanocomposites follows pseudo first order reaction kinetics, described by $ln\left(\frac{C}{C_0}\right) = Kt$, where K is the first order rate constant. The degradation rate for all the nanocomposites (Fig 6b,d, Fig 7b,d, Fig 8b), under visible and UV light are calculated and listed in Table S3. Among all, the maximum rate constant is observed for rGO-Fe_3O_4-TiO_2 nanocomposite under UV-light irradiation (K=0.56 min^{-1}). Furthermore, the stability as well as reusability of the synthesized nanocomposites were investigated by reusing the ternary rGO-Fe_3O_4-TiO_2 nanocomposite, as this is important from industrial point of view. For this, rGO-Fe_3O_4-TiO_2 nanocomposite was separated, washed and dried after the photocatalytic reaction and then reused for the next three run. The recycled adsorption behavior is shown in Fig.S3, where it is observed that, after being used for three times the dye removal efficiency is found to be 94% and 86% for UV and visible light irradiation, respectively. This indicates the good stability and reusability of the nanocomposites.

3.2 Adsorption analysis

Due to large specific surface area, high pore volume and pore size metal oxides provide excellent adsorption capabilities for hazardous anions such as phosphate, arsenate, fluoride etc. Having high porosity, metal oxides offer many adsorption sites for water adsorbed anions pollutant, which improve specific affinity of them towards anions. In addition, the existence of the large number of HO• present on the surface of anions also helps them to get adsorbed inside the metal

oxides [51]. After interacting with metal oxide surface, Arsenic ion undergoes through chemisorption process and reflects a tendency to form bidentate binuclear and monodentate two inner-sphere surface complex [52]. From BET results, it is cleared that the incorporation of Fe_3O_4 and TiO_2 metal oxides on rGO sheet increases specific surface area of resultant nanocomposite, which can lead to significant improvement in Arsenic removal efficiency. Thus to explore the adsorption capabilities of as-synthesized nanocomposites, the present study investigates the adsorption of As(III) metal ions upon Fe_3O_4 and TiO_2 nanoparticles attached over rGO, using different adsorption isotherms and kinetic model.

3.2.1 Adsorption Isotherm

The adsorption isotherm provides the important information about the interaction between the adsorption and adsorbate molecules, when adsorption process reaches on the equilibrium state. In the present study, Langmuir and Freundlich isotherm were used to fit the adsorption equilibrium data of As(III) adsorption on the nanocomposites [14]. The Langmuir and Freundlich isotherm are described as

$$\frac{C_e}{Q_e} = \frac{1}{K_L Q_M} + \left(\frac{1}{Q_M}\right) C_e \qquad (1)$$

$$lnQ_e = lnK_f + \frac{1}{n} lnC_e \qquad (2)$$

where in Langmuir isotherms (1), *Q*e is the amount of As(III) adsorbed per unit weight of adsorbent (mg/g), *C*e is the equilibrium concentration of As(III) (mg/L), K_L is the constant related to the free energy of adsorption (L/mg), and Q_m is the maximum adsorption capacity (mg/g). In Freundlich isotherms (2), K_f (L/mg) is the Freundlich parameter, while (1/n) is the adsorption intensity. The linear natures of Langmuir and Freundlich plots (Fig 9 a,b) indicate that adsorption of As(III) on nanocomposites follows both the isotherms with high correlation

coefficient (R^2). The value of adsorption parameters, evaluated from the slope and intercept, are listed in Table S4. The value of the Freundlich constant is found to be greater than 1, which implies that the adsorption of As(III) on nanocomposites is a favorable process [53]. These results also confirm that with increasing contamination adsorption rate also enhances. It is evident from Table S4 that rGO-Fe_3O_4-TiO_2 nanocomposite provides the maximum adsorption capacity (147.05 mg/g). From, BET results it is cleared that the incorporation of Fe_3O_4 and TiO_2 metal oxides on rGO increases the specific surface area of nanocomposites, which can lead to significant improvement in arsenic removal efficiency. Further, in rGO-Fe_3O_4-TiO_2, the synergetic interaction between Fe_3O_4 and TiO_2 can also enhance the adsorption capacity. Additionally, due to magnetic properties of Fe_3O_4, rGO-Fe_3O_4-TiO_2 can be easily separated from the contaminated water. The comparison of maximum monolayer adsorption capacity of As(III) onto various adsorbents, from literature, has been listed in Table 1. It is clear that the ternary rGO-Fe_3O_4-TiO_2 nanocomposite of the present study provides the highest adsorption capacity of 147.05 mg/g, compared to other adsorbents reported in the literature.

Table 1. Comparison of the maximum monolayer adsorption of As(III) onto various adsorbents obtained by Langmuir isotherms.

Adsorbent	q_{max} (mg/g)	Reference
Nanoscale zero valent iron (NZVI) –RGO	35.83	[54]
NZVI-actived carbon nanoparticles	18.2	[55]
Iron-containing ordered mesoporous carbon	9.3	[56]
Fe_3O4–rGO nanoparticles	13.1	[14]
Fe_3O_4–RGO–MnO_2 nanoparticles	14.04	[57]
Functionalized graphene sheets	138.79	[58]
ZrO ($(OH)_2$)-GO	95.15	[59]

rGO-TiO_2	10.6	Present work
rGO-Fe_3O_4	33.22	Present work
rGO-Fe_3O_4-TiO_2	147.05	Present work

3.2.2 Adsorption Kinetics

To study the adsorption kinetics, the experimental results obtained for the adsorbent were analyzed by using a pseudo-second-order kinetic model expressed as $\frac{t}{Q_t} = \frac{1}{Q_{eq}^2 K_1} + \left(\frac{1}{Q_{eq}}\right) t$ [49], where K_1 (g/mg min) is the rate constant of the pseudo-second-order model. Q_t (mg/g) and Q_{eq} (mg/g) are the amount of the As(III) adsorbed at time t (min) and equilibrium, respectively. Fig.10 (a, b) shows the adsorption of As(III) ions on nanocomposites, which implies that the adsorption increases significantly with increasing contact time. All the parameters along with correlation coefficient (R^2) and initial adsorption rate h_0, obtained from the plot of pseudo-second-order kinetic model, are shown in Table S5. The initial adsorption rate values were calculated by using the relation $h_0 = K_1 \times Q_e^2$ [60]. The high correlation coefficient values suggest that the adsorption kinetic of As(III) on nanocomposites follows the pseudo second order model, which affirms that adsorption of As(III) occurs through chemisorption process [61]. Further, the adsorption of As(III) on nanocomposites was also investigated by the intraparticle diffusion (IPD) model [62]. According to IPD model the initial rate of intraparticle diffusion is obtained by using the relation $Q_t = K_i t^{0.5}$, where Q_t (mg/g) is the amount of adsorbed metal ions at time t (min) on the nanocomposites and K_i (mg/g min^{-1}) is the IPD rate constant. Here, K_i is rate determining factor and obtained by the slope of the IPD relation. Fig.11 shows the adsorption of As(III) with square root of time, where the initial curved part can be attributed to the boundary layer diffusion effect [63] while the final linear portion might be due to the intraparticle diffusion effects. These results reveal that here, adsorption of As(III) ions involves

both boundary layer and intraparticle diffusion effect. K_i is a very important factor, which decides the rate of adsorption in the linear region of the curve. The obtained Ki values are given in Table S5, where the ternary nanocomposite (rGO-Fe_3O_4-TiO_2) shows the maximum IPD rate constant value.

4. Conclusions

In summary, a unique ternary nanocomposite, comprising of Fe_3O_4 and TiO_2 nanoparticles supported on rGO has been synthesized by using simple wet chemical method. Compared to binary (rGO-TiO_2/rGO-Fe_3O_4) nanocomposites, the ternary rGO-Fe_3O_4-TiO_2 nanocomposite shows excellent photocatalytic efficiency and high adsorption affinity for the removal of MB and As(III) from water. The MB degradation was evaluated under both UV and visible irradiation. Compared to bare TiO_2 and Fe_3O_4 nanoparticles, the nanocomposites show high dye degradation efficiency due to the synergetic interaction of metal oxides with rGO. The dye degradation efficiency is found to be more under UV-irradiation and the maximum rate degradation rate is observed for ternary nanocomposite ($k=0.58\ min^{-1}$). Langmuir adsorption isotherm suggests that the ternary nanocomposite owns maximum adsorption capacity 147.05 (mg/g) for As(III) metal ions. The obtained adsorption kinetic data are found to be linearly well fitted with the pseudo-second-order model. Due to the striking features of ternary nanocomposites (rGO-Fe_3O_4-TiO_2), it can be efficiently used for many applications, especially in wastewater treatment.

Acknowledgment

This work is financially supported by Department of Science and Technology India.

References

[1] R. K. Upadhyay, N. Soin and S. S. Roy, *RSC Adv.*, 2014, **4**, 3823-3851.

[2] T. Robinson, G. McMullan, R. Marchant and P. Nigam, *Bioresour. Technol.*, 2001, **77**, 247-255.

[3] B. Prasad, C. Ghosh, A. Chakraborty, N. Bandyopadhyay and R. Ray, *Desalination*, 2011, **274**, 105-112.

[4] P. Benjwal and K. K. Kar, *J. Environ. Chem.Eng.*, 2015, **3**, 2076-2083.

[5] A. K. Geim, *Science*, 2009, **324**, 1530-1534.

[6] V. K. K. Upadhyayula, S. Deng, M. C. Mitchell and G. B. Smith, *Sci. Total Environ.*, 2009, **408**, 1-13.

[7] G. Jiang, Z. Lin, C. Chen, L. Zhu, Q. Chang, N. Wang, W. Wei and H. Tang, *Carbon*, 2011, **49**, 2693-2701.

[8] X. An and J. C. Yu, *RSC Adv.*, 2011, **1**, 1426-1434.

[9] C. Shan, H. Yang, D. Han, Q. Zhang, A. Ivaska and L. Niu, *Langmuir*, 2009, **25**, 12030-12033.

[10] X. Yang, C. Chen, J. Li, G. Zhao, X. Ren and X. Wang, *RSC Adv.*, 2012, **2**, 8821-8826.

[11] D. Wang, R. Kou, D. Choi, Z. Yang, Z. Nie, J. Li, L. V. Saraf, D. Hu, J. Zhang and G. L. Graff, *ACS Nano*, 2010, **4**, 1587-1595.

[12] S. Wang, S. P. Jiang and X. Wang, *Electrochim. Acta*, 2011, **56**, 3338-3344.

[13] D. Long, W. Li, L. Ling, J. Miyawaki, I. Mochida and S.-H. Yoon, *Langmuir*, 2010, **26**, 16096-16102.

[14] V. Chandra, J. Park, Y. Chun, J. W. Lee, I.-C. Hwang and K. S. Kim, *ACS Nano*, 2010, **4**, 3979-3986.

[15] P. Mandal and A. P. Chattopadhyay, *Dalton Trans.*, 2015, **44**, 11444-11456.

[16] H. Sun, L. Cao and L. Lu, *Nano. Res.*, 2011, **4**, 550-562.

[17] C. T. Yavuz, J. Mayo, W. Y. William, A. Prakash, J. C. Falkner, S. Yean, L. Cong, H. J. Shipley, A. Kan and M. Tomson, *Science*, 2006, **314**, 964-967.

[18] P. Benjwal and K. K. Kar, *Mater. Chem. Phys.*, 2015, **160**, 279-288.

[19] G. Williams, B. Seger and P. V. Kamat, *ACS Nano*, 2008, **2**, 1487-1491.

[20] Q. Xiang and J. Yu, *J. Phys. Chem. lett*, 2013, **4**, 753-759.

[21] X.-X. Wei, C.-M. Chen, S.-Q. Guo, F. Guo, X.-M. Li, X.-X. Wang, H.-T. Cui, L.-F. Zhao and W. Li, *J. Mater. Chem. A*, 2014, **2**, 4667-4675.

[22] Y. Wang, J. Yu, W. Xiao and Q. Li, *J. Mater. Chem. A*, 2014, **2**, 3847-3855.

[23] W. S. Hummers Jr and R. E. Offeman, *J. Am. Chem. Soc.*, 1958, **80**, 1339-1339.

[24] C. Santhosh, P. Kollu, S. Doshi, M. Sharma, D. Bahadur, M. T. Vanchinathan, P. Saravanan, B.-S. Kim and A. N. Grace, *RSC Adv.*, 2014, **4**, 28300-28308.

[25] L.-L. Tan, W.-J. Ong, S.-P. Chai and A. R. Mohamed, *Nanoscale Res Lett*, 2013, **8**, 1-9.

[26] S. D. Perera, R. G. Mariano, K. Vu, N. Nour, O. Seitz, Y. Chabal and K. J. Balkus Jr, *ACS Catal.*, 2012, **2**, 949-956.

[27] X. Yang, X. Zhang, Y. Ma, Y. Huang, Y. Wang and Y. Chen, *J. Mater. Chem.*, 2009, **19**, 2710-2714.

[28] Z. Xiong, L. L. Zhang, J. Ma and X. Zhao, *Chem. Commun.*, 2010, **46**, 6099-6101.

[29] S. Stankovich, D. A. Dikin, G. H. Dommett, K. M. Kohlhaas, E. J. Zimney, E. A. Stach, R. D. Piner, S. T. Nguyen and R. S. Ruoff, *Nature*, 2006, **442**, 282-286.

[30] Y.-J. Xu, Y. Zhuang and X. Fu, *J. Phys. Chem. C*, 2010, **114**, 2669-2676.

[31] W. Yan, F. He, S. Gai, P. Gao, Y. Chen and P. Yang, *J. Mater. Chem. A*, 2014, **2**, 3605-3612.

[32] J. Cherusseri and K. K. Kar, *RSC Adv.*, 2015, **5**, 34335-34341.

[33] R. Sharma and K. K. Kar, *J. Mater. Chem. A*, 2015, **3**, 11948-11959.

[34] Y. Jiang, Z.-J. Jiang, L. Yang, S. Cheng and M. Liu, *J. Mater. Chem. A*, 2015, **3**, 11847-11856.

[35] V. Štengl, S. Bakardjieva, T. M. Grygar, J. Bludská and M. Kormunda, *Chem. Cent. J*, 2013, **7**, 41.

[36] M. Zong, Y. Huang, Y. Zhao, X. Sun, C. Qu, D. Luo and J. Zheng, *RSC Adv.*, 2013, **3**, 23638-23648.

[37] C. Gómez-Navarro, R. T. Weitz, A. M. Bittner, M. Scolari, A. Mews, M. Burghard and K. Kern, *Nano Lett.*, 2007, **7**, 3499-3503.

[38] J. Paredes, S. Villar-Rodil, A. Martinez-Alonso and J. Tascon, *Langmuir*, 2008, **24**, 10560-10564.

[39] Y. Zhang and C. Pan, *J. Mater. Sci.*, 2011, **46**, 2622-2626.

[40] N. Yang, J. Zhai, D. Wang, Y. Chen and L. Jiang, *ACS Nano*, 2010, **4**, 887-894.

[41] G. Jung and H. I. Kim, *J. Appl. Polym. Sci.*, 2014, **131**,

[42] J. Su, M. Cao, L. Ren and C. Hu, *J. Phys. Chem. C*, 2011, **115**, 14469-14477.

[43] J. Zhang, Z. Xiong and X. Zhao, *J. Mater. Chem.*, 2011, **21**, 3634-3640.

[44] G. T. S. How, A. Pandikumar, H. N. Ming and L. H. Ngee, *Sci. Rep.*, 2014, **4**,

[45] W. Jiang, K.-L. Lai, H. Hu, X.-B. Zeng, F. Lan, K.-X. Liu, Y. Wu and Z.-W. Gu, *J. Nanopart. Res.*, 2011, **13**, 5135-5145.

[46] T. Daou, G. Pourroy, S. Begin-Colin, J. Greneche, C. Ulhaq-Bouillet, P. Legare, P. Bernhardt, C. Leuvrey and G. Rogez, *Chem. Mater.*, 2006, **18**, 4399-4404.

[47] Y. Dai, Y. Jing, J. Zeng, Q. Qi, C. Wang, D. Goldfeld, C. Xu, Y. Zheng and Y. Sun, *J. Mater. Chem.*, 2011, **21**, 18174-18179.

[48] D. Ravelli, D. Dondi, M. Fagnoni and A. Albini, *Chem. Soc. Rev.*, 2009, **38**, 1999-2011.

[49] T. Peik-See, A. Pandikumar, L. H. Ngee, H. N. Ming and C. C. Hua, *Catal. Sci. Techno*, 2014, **4**, 4396-4405.

[50] B. Jiang, C. Tian, Q. Pan, Z. Jiang, J.-Q. Wang, W. Yan and H. Fu, *J. Phys. Chem. C*, 2011, **115**, 23718-23725.

[51] Q. Jiuhui, *J. Environ. Sci.*, 2008, **20**, 1-13.

[52] C. Luengo, M. Brigante and M. Avena, *J. Colloid Interface Sci.*, 2007, **311**, 354-360.

[53] R. Kumar, J. Rashid and M. Barakat, *RSC Adv.*, 2014, **4**, 38334-38340.

[54] C. Wang, H. Luo, Z. Zhang, Y. Wu, J. Zhang and S. Chen, *J. Hazard. Mater.*, 2014, **268**, 124-131.

[55] H. Zhu, Y. Jia, X. Wu and H. Wang, *J. Hazard. Mater.*, 2009, **172**, 1591-1596.

[56] Z. Gu, B. Deng and J. Yang, *Microporous Mesoporous Mater.*, 2007, **102**, 265-273.

[57] X. Luo, C. Wang, S. Luo, R. Dong, X. Tu and G. Zeng, *Chem. Eng. J.*, 2012, **187**, 45-52.

[58] A. K. Mishra and S. Ramaprabhu, *Desalination*, 2011, **282**, 39-45.

[59] X. Luo, C. Wang, L. Wang, F. Deng, S. Luo, X. Tu and C. Au, *Chem. Eng. J.*, 2013, **220**, 98-106.

[60] Y. S. Ho and G. McKay, *Chem. Eng. J.*, 1998, **70**, 115-124.

[61] T. Wen, X. Wu, X. Tan, X. Wang and A. Xu, *ACS Appl. Mater. Interfaces*, 2013, **5**, 3304-3311.

[62] W. J. Weber and J. C. Morris, *J. Sanit.Eng. Div.*, 1963, **89**, 31-60.

[63] C. Chang, W. Tsai, C. Ing and C. Chang, *J. Colloid Interface Sci.*, 2003, **260**, 273-279.

Figures with Captions:

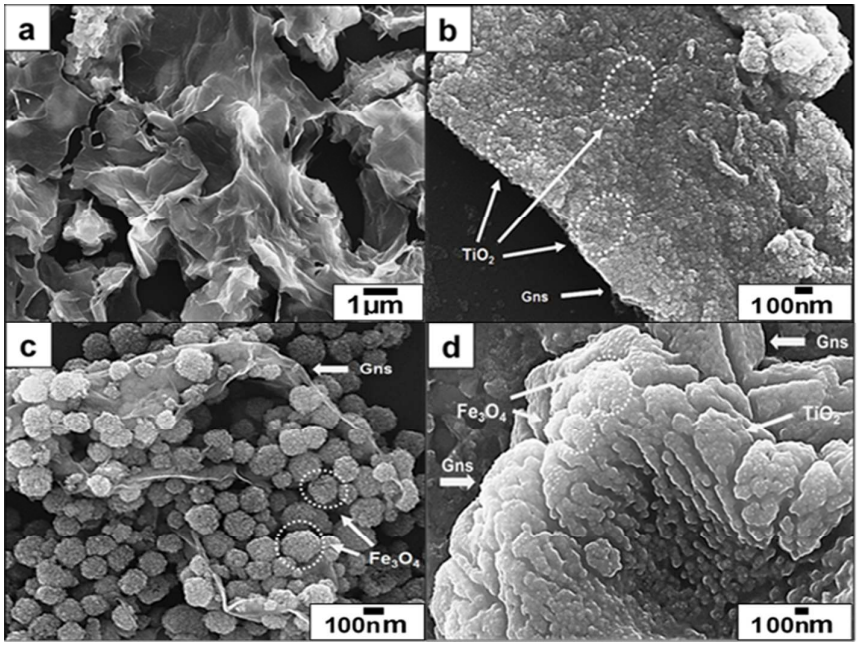

Fig. 1. FESEM images of (a) GO, (b) rGO-TiO_2, (c) rGO-Fe_3O_4, and (d) rGO-Fe_3O_4-TiO_2.

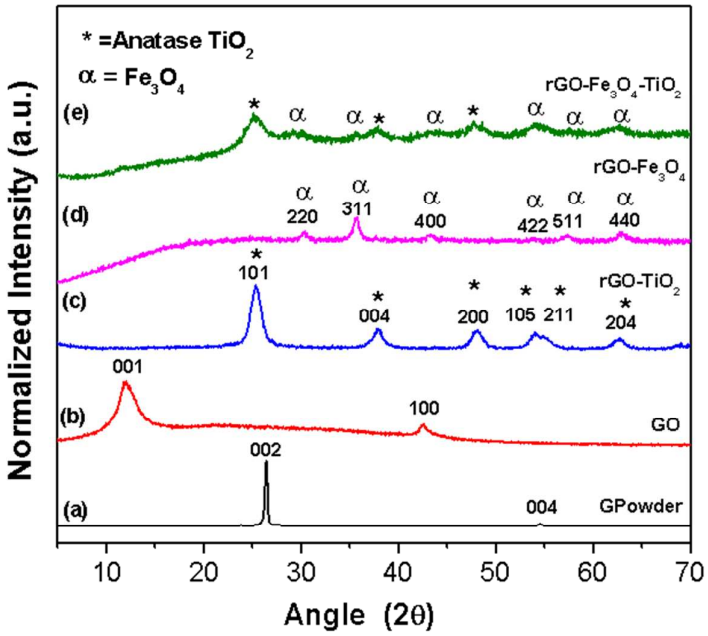

Fig. 2. XRD patterns of (a) graphite powder, (b) GO, (c) rGO-TiO_2, (d) rGO-Fe_3O_4 and (e) rGO-Fe_3O_4-TiO_2.

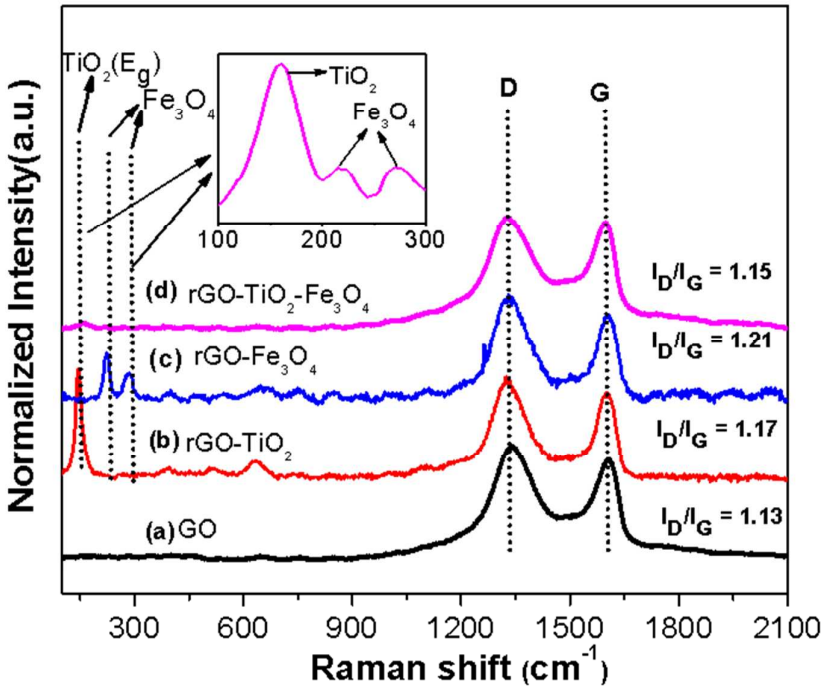

Fig. 3. Raman spectra of (a) GO, (b) rGO-TiO_2, (c) rGO-Fe_3O_4 and (d) rGO-Fe_3O_4-TiO_2.

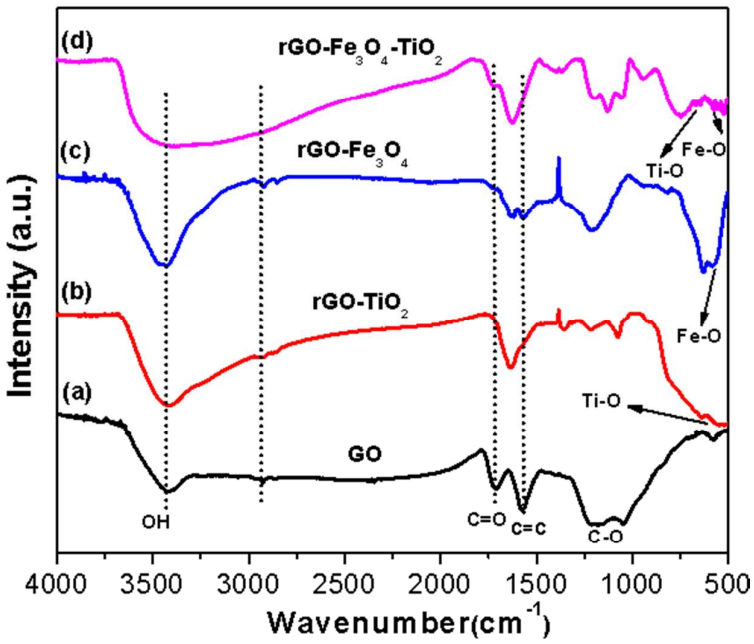

Fig. 4. FTIR spectra of (a) GO, (b) rGO-TiO_2, (c) rGO-Fe_3O_4 and (d) rGO-Fe_3O_4-TiO_2.

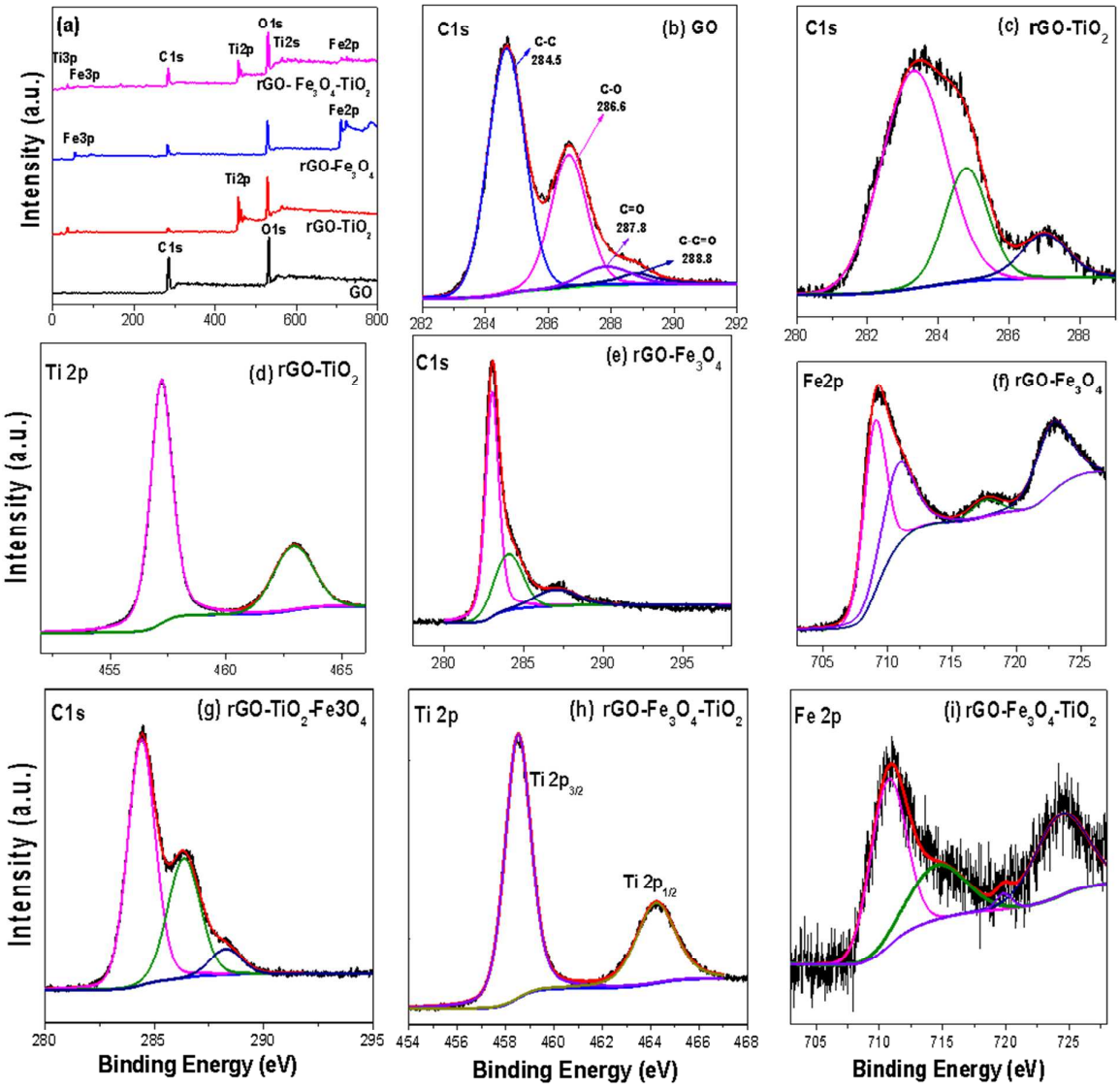

Fig. 5. (a) XPS survey scan of GO, binary and ternary nanocomposite. The high-resolution XPS spectrum of (b) C1s of GO, and (c-f) C1s, Ti2p, Fe2p and O1s of binary and ternary nanocomposite.

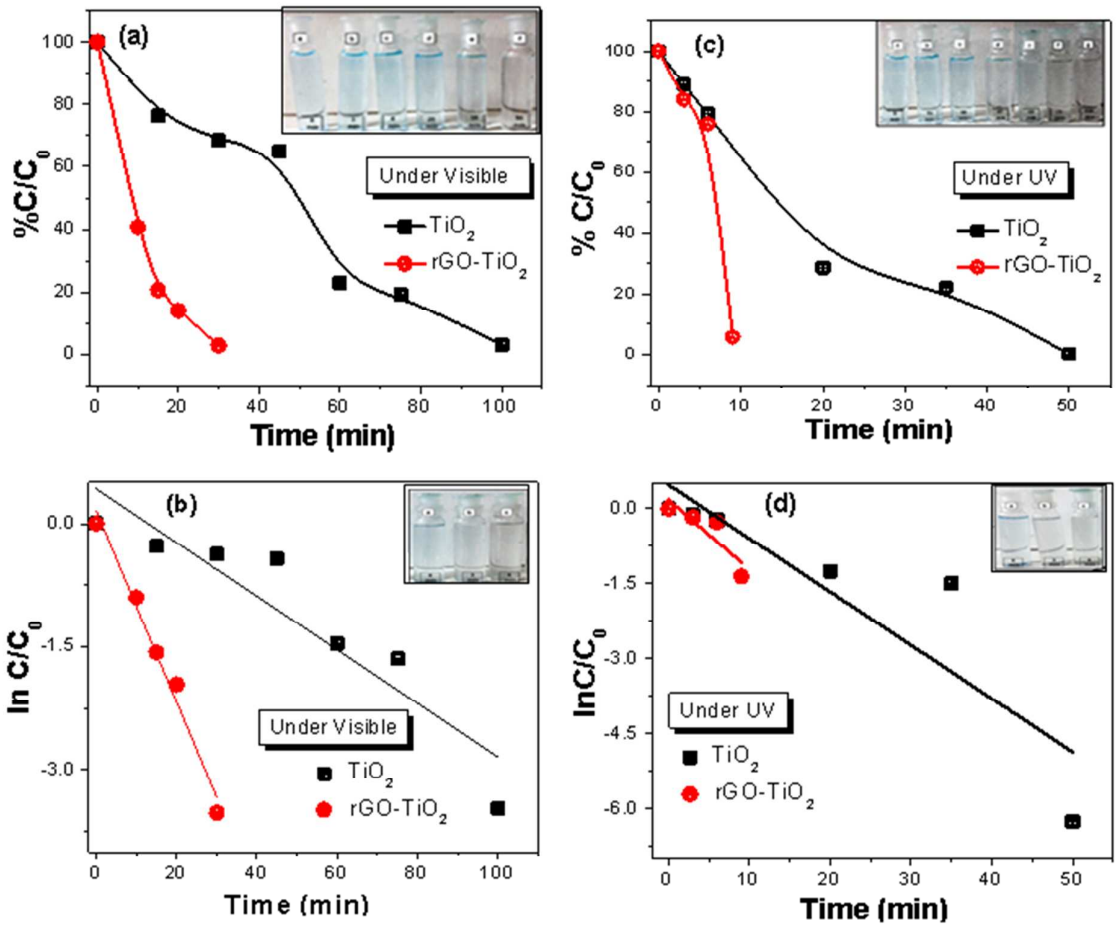

Fig. 6. Change in concentration and rate kinetics for photocatalytic degradation of MB with time by TiO_2 and rGO-TiO_2 (a-b) in presence of visible light irradiation and (c-d) in presence of UV. Insets show the digital image of MB degradation in presence of visible light irradiation by (a) TiO_2, (b) rGO-TiO_2 and in presence of UV light irradiation by (c) TiO_2 and (d) rGO-TiO_2.

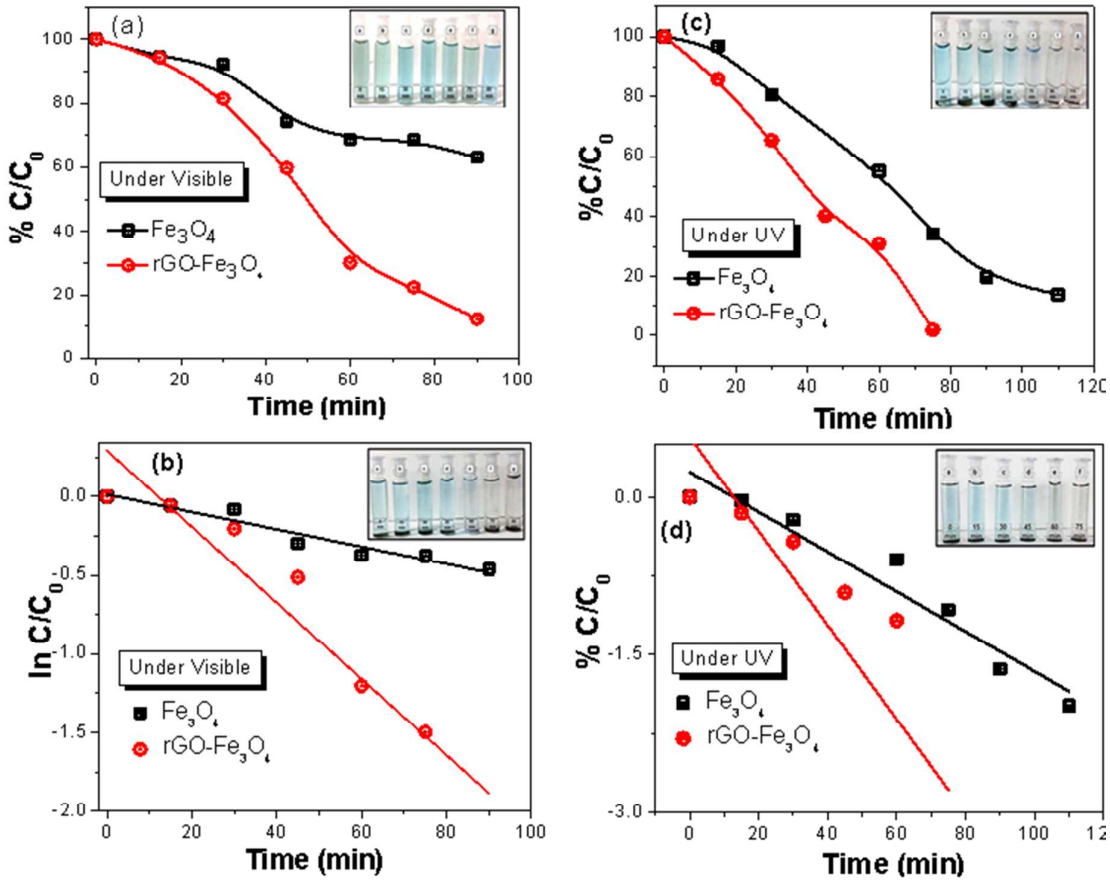

Fig. 7. Change in concentration and rate kinetics for photocatalytic degradation of MB with time by TiO_2 and rGO-Fe_3O_4 in presence of visible light irradiation (a-b) and UV (c-d). Insets show the digital image of MB degradation in presence of visible light irradiation by (a) Fe_3O_4, (b) rGO-Fe_3O_4 and in presence of UV light irradiation by (c) Fe_3O_4 and (d) rGO-Fe_3O_4.

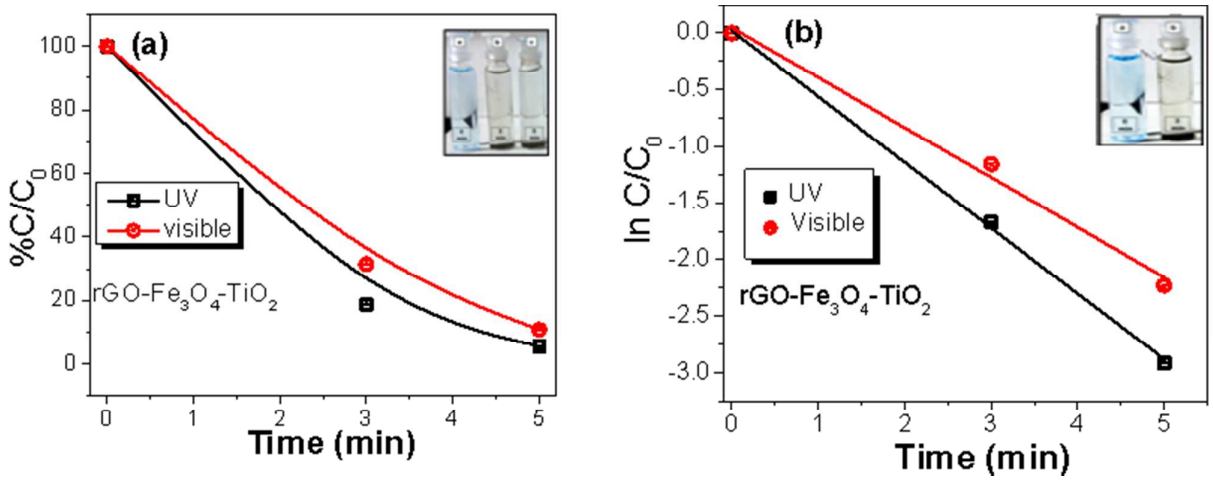

Fig. 8. (a) Photocatalytic degradation of MB and (b) rate kinetic photodegradation of ternary rGO-Fe_3O_4-TiO_2 nanocomposite, under the presence of visible and UV light irradiation. Insets of (a) and (b) show the digital image of MB degradation by rGO-Fe_3O_4-TiO_2 in presence of visible light and UV light irradiation, respectively.

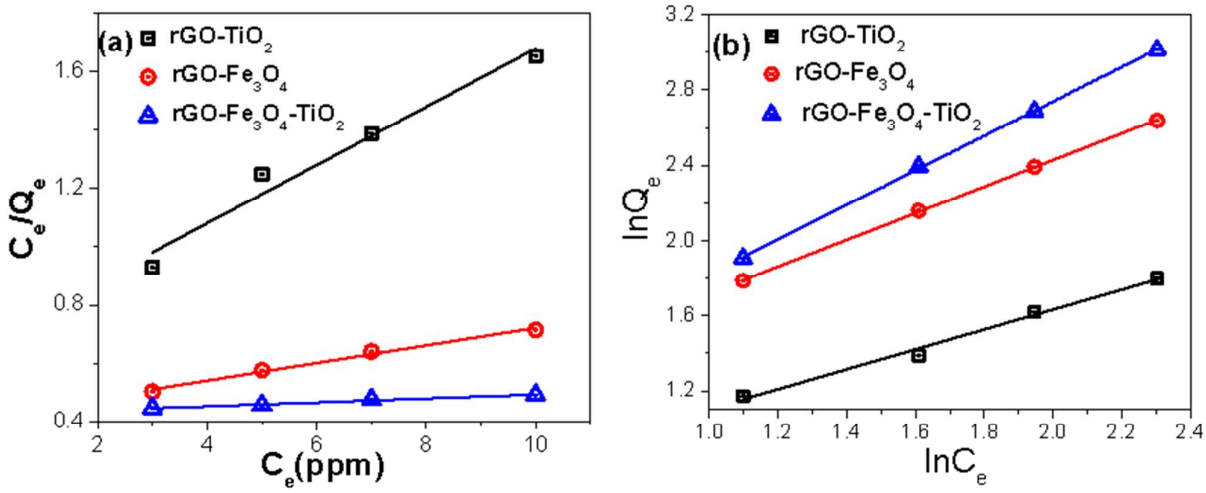

Fig. 9. (a) Langmuir and (b) Freundlich adsorption isotherm plots of As(III) adsorption on nanocomposites at room temperature (pH~7.0).

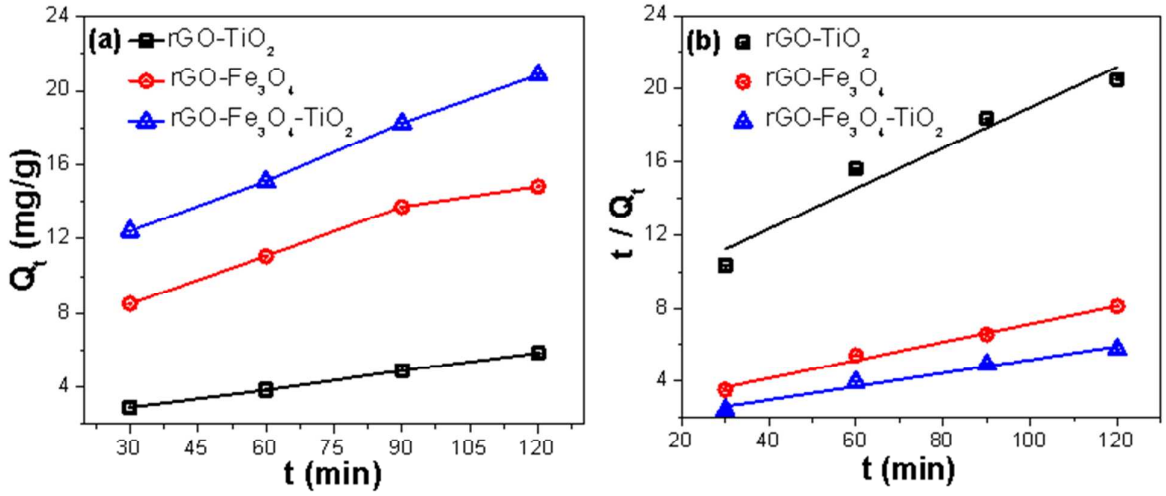

Fig.10. Adsorption kinetics for As(III) onto nanocomposites at room temperature (pH~7) by using pseudo second order kinetic model.

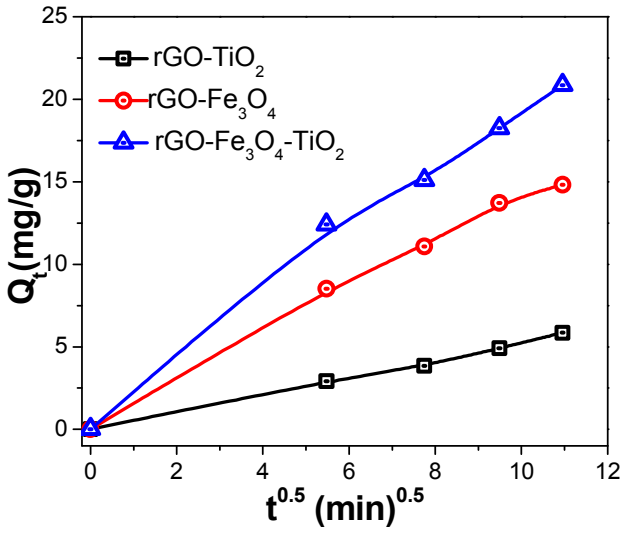

Fig. 11. Intraparticle diffusion model plot of As(III) adsorption on nanocomposites at room temperature (pH~7).